

Engineering Relaxation Pathways in Building Blocks of Artificial Spin Ice for Computation


H. Arava,^{1,2,*} N. Leo,^{1,2,†,‡} D. Schildknecht,^{1,2,3} J. Cui,^{1,2} J. Vijayakumar,⁴ P. M. Derlet,³ A. Kleibert,⁴ and L. J. Heyderman^{1,2}

¹Laboratory for Mesoscopic Systems, Department of Materials, ETH Zurich, 8093 Zurich, Switzerland

²Laboratory for Multiscale Materials Experiments, Paul Scherrer Institute, 5232 Villigen PSI, Switzerland

³Condensed Matter Theory Group, Paul Scherrer Institute, 5232 Villigen PSI, Switzerland

⁴Swiss Light Source, Paul Scherrer Institute, 5232 Villigen PSI, Switzerland

 (Received 17 December 2018; revised manuscript received 21 March 2019; published 31 May 2019)

Nanomagnetic logic, which makes use of arrays of dipolar-coupled single-domain nanomagnets for computation, holds promise as a low-power alternative to traditional computation with CMOS. Beyond the use of nanomagnets for Boolean logic, nanomagnets can also be exploited for nondeterministic computational schemes such as edge detection in images and for solving the traveling salesman problem. Here, we demonstrate the potential of arrangements of thermally active nanomagnets based on artificial spin ice for both deterministic and probabilistic computation. This is achieved by engineering structures that follow particular thermal relaxation pathways consisting of a sequence of reorientations of magnet moments from an initial field-set state to a final low-energy output state. Additionally, we demonstrate that it is possible to tune the probability of attaining a particular final low-energy state, and therefore the likelihood of a given output, by modifying the intermagnet distance. Finally, we experimentally demonstrate a scheme to connect several computational building blocks for complex computation.

DOI: [10.1103/PhysRevApplied.11.054086](https://doi.org/10.1103/PhysRevApplied.11.054086)

I. INTRODUCTION

All-magnetic computation with arrays of dipolar-coupled nanomagnets has the potential to provide a low-power alternative to existing CMOS technologies [1–6]. In the last decade, significant progress has been made in the use of nanomagnets for deterministic computation, which is often referred to as nanomagnetic logic, where nanomagnets with in-plane [1,2,7] and perpendicular anisotropy [8] are implemented to perform Boolean operations. Here, it is the two stable magnetic configurations associated with each magnet that can be used to encode binary information.

A variety of approaches have been developed to apply nanomagnets to computation, including strain-mediated logic [9], spin-Hall-induced effects [10], and their three-dimensional implementation [11]. In addition, a high clocking speed in a chain of dipolar coupled nanomagnets was achieved using a pulsed current to transfer information at ultrafast timescales [12]. Beyond Boolean computation, novel computational schemes with nanomagnets have emerged such as designing arrays of nanomagnets where the relaxation to a low-energy state after the application of

a field can be implemented for image recognition [13] or using coupled randomly switching nanomagnets to solve, for example, the traveling salesman problem [14].

The exploitation of more complex arrangements of nanomagnets such as those found in artificial spin ice, where nanomagnets are placed on the sites of a periodic lattice such as a square [15] or kagome lattice [16], brings advantages such as an improved reliability of computation, which we have demonstrated in structures based on artificial square ice [17]. In order to exploit artificial spin ice structures for applications, it is useful to be able to access specific moment configurations. This has been achieved, for example, in small artificial kagome spin ice structures consisting of up to three hexagonal rings of nanomagnets with specific field protocols [16] or by modifying the shape of individual nanomagnets [18]. Other avenues to access specific magnetic states in artificial spin ice involved the use of a specialized magnetic tip [19,20]. Finally, there have been proposals to use artificial kagome spin ice structures [21] as well as to combine multiple three-moment logic gates in treelike circuits [22] for computation.

In this work, we control the energy landscape associated with artificial spin ice, engineering the relaxation pathways in structures containing arrays of thermally active dipolar-coupled nanomagnets. These relaxation pathways consist of a sequence of reorientations of the nanomagnet moments as the structures relax from an initial field-set

*hanu@pm.me

†n.leo@nanogune.eu

‡Present address: CIC nanoGUNE, 20018 Donostia-San Sebastián, Spain.

state to a final low-energy state. Based on measurements of the thermal evolution of the magnetic configurations, as well as kinetic Monte Carlo simulations, we identify two distinct types of pathways in the energy landscape that are either deterministic or probabilistic. For a deterministic relaxation from an initial field-set state, the final state is expected to always be a particular low-energy state. In contrast, for probabilistic relaxation, there are two or more possible final low-energy states, which occur with a certain probability in a particular time frame.

Here, we present strategies to tune the probability of accessing low-energy states. Finally, we experimentally demonstrate a way to integrate individual computational units into large circuits. With this, we provide a foundation for the implementation of artificial spin ice for deterministic and probabilistic computation.

II. BACKGROUND

Because of their shape anisotropy, elongated nanomagnets made from soft magnetic materials, such as permalloy ($\text{Ni}_{80}\text{Fe}_{20}$), form single-domain states with a net magnetic moment pointing along the long axis of the nanomagnet and, thus, can be represented by macrospins with Ising degrees of freedom. For arrangements of dipolar-coupled

nanomagnets such as those shown in Fig. 1, the interaction potential, assuming point-dipole-like moments, is given by

$$V(\mathbf{r}_{ij}, \mathbf{m}_i, \mathbf{m}_j) = -\frac{\mu_0}{4\pi r_{ij}^3} [3(\mathbf{m}_i \cdot \hat{\mathbf{r}}_{ij})(\mathbf{m}_j \cdot \hat{\mathbf{r}}_{ij}) - \mathbf{m}_i \cdot \mathbf{m}_j], \quad (1)$$

with the distance vector \mathbf{r}_{ij} separating the magnetic point dipoles \mathbf{m}_i and \mathbf{m}_j and $\hat{\mathbf{r}}_{ij} = \mathbf{r}_{ij}/|\mathbf{r}_{ij}|$. The total energy of an arrangement of N macrospins is then given by $E_{\text{total}} = (1/2) \sum_{i,j=1}^N V(\mathbf{r}_{ij}, \mathbf{m}_i, \mathbf{m}_j)$. Dipolar interactions favor flux-closure head-to-tail configurations, whereas head-to-head or tail-to-tail configurations are energetically unfavorable. Furthermore, the dynamics of thermally assisted, spontaneous moment reorientations of individual nanomagnets is described by a transition rate, which is given by the moment reorientation rate $\nu(E_T, T)$, where

$$\nu(E_T, T) = \nu_0 e^{-\frac{E_T}{k_B T}}. \quad (2)$$

Here, ν_0 is the attempt frequency, k_B is the Boltzmann constant, and T the temperature. The barrier energy $E_T = E_b + (1/2)\Delta E_{m \rightarrow l}$ is the energy required for a single nanomagnet in the array to switch, and includes the

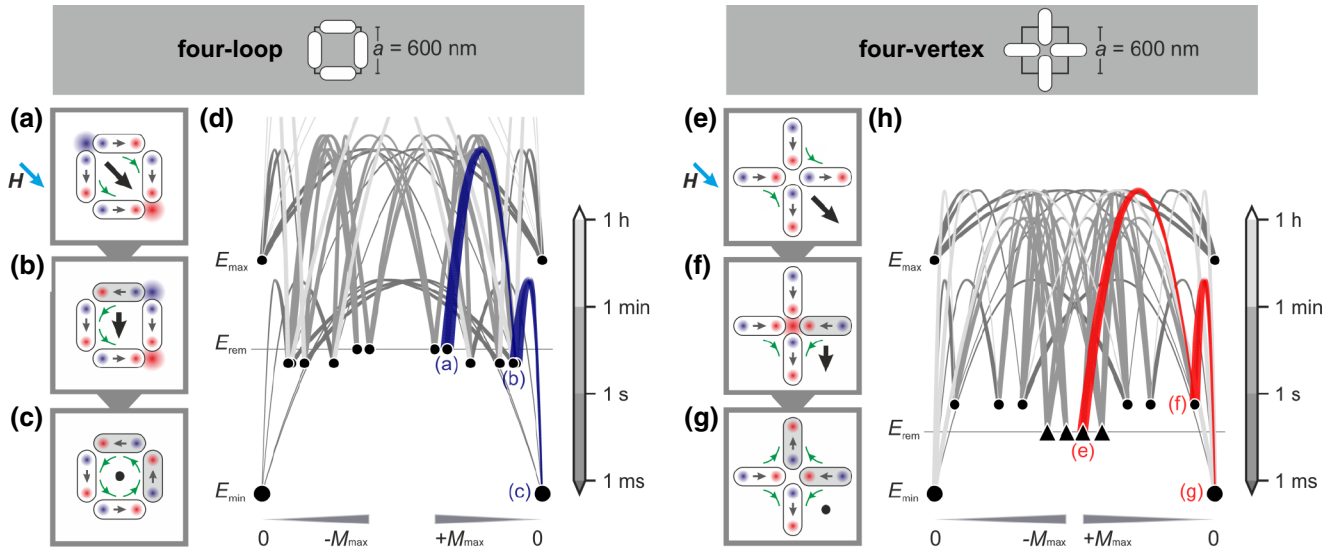


FIG. 1. Thermal relaxation and state network diagrams for four-loop and four-vertex structures. (a)–(c) Thermal relaxation in a four-loop structure from a field-set state to one of the two degenerate flux-closure ground states. Switched magnets are highlighted in gray, head-to-tail arrangements are indicated by green arrows, and the net magnetization is indicated by black arrows. (d) State network diagram for the four-loop structure. The states are indicated with black points that are located according to their energies along the vertical axis and the net magnetization of the state along the horizontal axis. Transitions between states m and l via single-nanomagnet reorientations are indicated by tapered lines. The midpoint of the lines corresponds to the energy $E_m + E_T$, where the barrier energy $E_T = E_b + (1/2)(E_l - E_m)$. The grayscale of the lines corresponds to the transition rate at $T = 400$ K according to Eq. (2) and the grayscale bar. The blue line represents the transitions between the states shown in (a)–(c), resulting in a monotonic relaxation path with successive lowering of dipolar energy. (e)–(g) In a four-vertex structure, thermal relaxation from a field-set state to the ground state requires a transition to a state of higher dipolar energy, which is associated with the creation of a magnetic charge at the vertex highlighted in red in panel (f). (h) State network diagram for the four-vertex structure. The red intermittent path is for the state evolution shown in (e)–(g), where an intermediate state with higher dipolar energy is accessed. The metastable states are indicated with triangles, while the ground states are indicated with larger black points.

single-nanomagnet switching barrier energy E_b and the difference in dipolar energy $\Delta E_{m \rightarrow l}$ between the initial and final nanomagnetic states m and l [23,24]. In the limit of low temperatures, the reorientation dynamics are slow, and thermal relaxation from an initial state toward a state of lower dipolar energy proceeds via successive reversals of individual magnetic moments. In configuration space, the system will therefore follow a path that is defined by a sequence of single-moment reversals. Such relaxation paths have a sequence of moment reorientations that can be classified into two categories: monotonic and intermittent. For a monotonic relaxation path, every moment reorientation results in a reduction of dipolar energy, i.e., $E_{i+1} < E_i$ for all states i . In contrast, intermittent relaxation paths are characterized by the presence of at least one transition to a higher-energy state, i.e., $E_{i+1} > E_i$ for at least one i . Because of the exponential relationship between the transition rate and the barrier energy in Eq. (2), transitions toward states of higher dipolar energy are kinetically suppressed.

Whether the paths are monotonic or intermittent strongly depends on the spatial arrangement of the nanomagnets. This dependence is illustrated by the relaxation behavior from an initial field-set configuration to the ground state for two basic motifs with four nanomagnets derived from artificial square ice [15] shown in Fig. 1. For the four-loop structure shown in Figs. 1(a)–1(c), the nanomagnets are arranged in a loop, and for the four-vertex structure shown in Figs. 1(e)–1(g), the nanomagnets meet at a common vertex. In both cases, the initial field-set state with energy E_{rem} is set by applying a magnetic field \mathbf{H} , indicated by a blue arrow in Figs. 1(a) and 1(e). On removing the field, the individual nanomagnets undergo thermally induced moment reorientations and the nanomagnet structure will relax to a ground state with minimal energy E_{min} . For the four-loop structure, the progression from the initial to the final, low-energy flux-closure state [Figs. 1(a)–1(c)] involves the successive lowering of dipolar energy and is thus a monotonic relaxation path. In contrast, the relaxation of the four-vertex structure to the ground state [Figs. 1(e)–1(g)] requires a transition from a state with one head-to-head and one tail-to-tail interaction [Fig. 1(e)] to a state with three head-to-head arrangements of the magnetic moments [fig. 1(f)]. This transition is associated with an increase in energy and thus results in an intermittent relaxation path. Each individual magnetic moment can be represented by a positive and negative magnetic charge (indicated as red and blue points on the nanomagnets). For the magnetic configurations shown in Figs. 1(e) and 1(g), there are two positive and two negative charges at the vertex and, therefore, no net charge, whereas the higher-energy configuration in Fig. 1(f) is associated with a net charge at the vertex highlighted in red.

The relaxation paths between different states can be depicted using a state network diagram for the energy

landscape, as shown in Figs. 1(d) and 1(h) for the four-loop and the four-vertex structures, respectively. Here, the states are indicated with black points and are located according to their energies E_{total} along the vertical axis and the net magnetization of the state $\pm|\mathbf{M}| = |\sum_i^N \mathbf{m}_i|$ along the horizontal axis. The sign of $\pm|\mathbf{M}|$ indicates whether \mathbf{M} is parallel or antiparallel to the initial applied field \mathbf{H} [blue arrows in Figs. 1(a) and 1(e)], with $-M_{\text{max}}$ and $+M_{\text{max}}$ indicating each extreme of net magnetization. E_{max} and E_{min} on the vertical axis indicate moment configurations with highest and lowest dipolar energies, while E_{rem} corresponds to an initial field-set state. Furthermore, it should be noted that an arbitrary offset along the horizontal axis is added to every point in order to avoid overlap of degenerate states. Single-moment-reversal connections between states m and l are represented by tapered lines, where the path is traveled from the wide end to the narrow end. The energy at the center of each line corresponds to $E_m + E_l$. The grayscale of the line indicates the transition rate $\nu(E_T, T)$ at $T = 400$ K according to Eq. (2) and calculated using the parameters specified in Sec. III.

Boolean operations can be realized with nanomagnet structures exhibiting a monotonic relaxation pathway, which guides the relaxation toward a specific final state. In contrast, intermittent relaxation pathways lead to a probability of achieving particular low-energy states, which can be implemented in computational schemes where weighted outputs are desired, such as artificial neural networks. It should be noted that relaxation pathways may incorporate metastable states, indicated by triangles in Fig. 1(h), which restrict subsequent single-moment reversals corresponding to transitions to configurations of higher dipolar energy. Relaxation pathways involving such metastable states are therefore of the intermittent type.

III. METHODS

Arrays of elongated permalloy nanomagnets, with a length of 470 nm and a width of 170 nm, are fabricated on a silicon substrate using electron-beam lithography in combination with lift-off processing. The nanomagnet arrangements in this work are based on an artificial square ice design, with the nanomagnet center-to-center distance $a = 600$ nm (see Fig. 1). In order to experimentally observe the thermal relaxation, in particular the individual moment reorientations at an accessible timescale, the nanomagnet arrays are fabricated from a permalloy wedge film with a thickness ranging from 1 to 15 nm over a distance of 6 μm , which is deposited using thermal evaporation at a base pressure of 2×10^{-6} mbar and capped with 2 nm of aluminum to prevent oxidation.

Magnetic imaging of the nanomagnet arrays is performed using x-ray photoemission electron microscopy (XPEEM), which makes use of resonant x-ray magnetic circular dichroism (XMCD) at the Fe L_3 edge to obtain

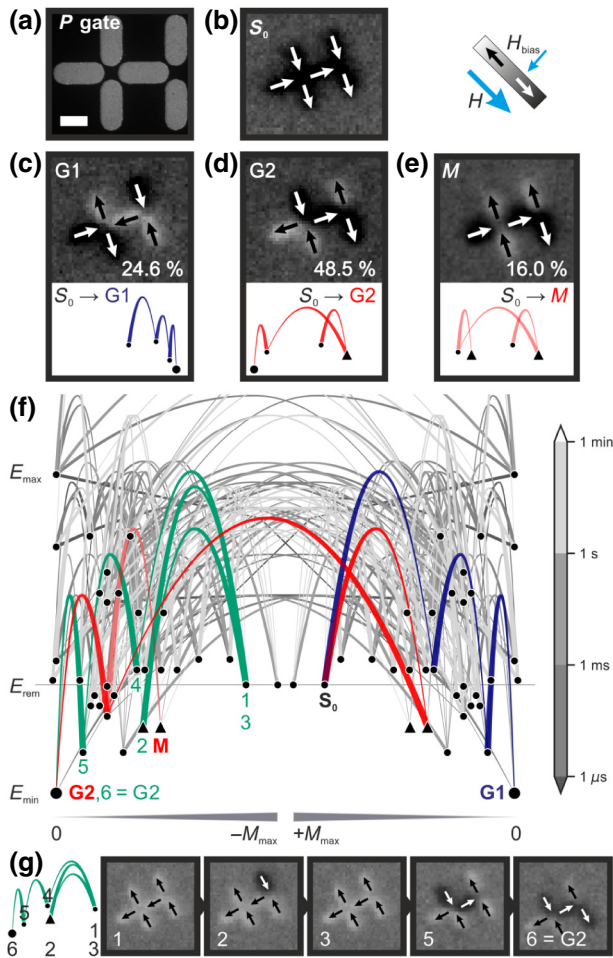


FIG. 2. Thermal relaxation and state network diagram of the P gate. (a) Scanning-electron microscopy (SEM) image of the P gate. The scale bar measures 250 nm. (b) Field-set initial state S_0 , degenerate ground states (c) G1 and (d) G2, and metastable state (e) M , imaged by XPEEM. For 390 gates, G1 is reached in 24.6% of the gates, whereas G2 is reached in 48.5% of the gates. In addition, 16.0% of the gates get stuck in the metastable state M . The relaxation path taken is determined by the height of the successive activation barriers that need to be overcome during relaxation. (f) State network diagram of the P gate at $T=295$ K. The fastest relaxation path from the field-set state S_0 to the ground states G1 and G2, represented by the larger black points, are intermittent paths highlighted in blue and red. (g) Many different relaxation paths can be explored and there can even be a reversal of direction with the system traveling back along a given path. This reversal is illustrated with successive XPEEM imaging of the relaxation from an initial field-set state (1) to a final low-energy state (6). Here, a change in direction of relaxation is observed when transitioning from (1) to (2) to (3) and, subsequently, the structure traverses the path to G2. The corresponding path in (f) is highlighted in green. In the XPEEM images, black and white arrows indicate the magnetic moment orientations.

magnetic contrast [25]. A pixelwise division of the images acquired with right and left circularly polarized incident x-rays gives a contrast that corresponds to the orientation

of the magnetic moments. For observations of thermal relaxation, a particular film thickness at a given temperature is chosen with moment reorientations at a second to minutes timescale, so that magnetic configurations between moment reorientations can be imaged.

The following experimental protocol is implemented to probe thermal relaxation behavior in different arrangements of nanomagnets. After field-setting the nanomagnets, so that all moments align toward the direction of the applied magnetic field, the sample is heated in order to assist thermal relaxation to a state of lower dipolar energy [17,26]. The final configurations are imaged with XPEEM for a large number of equivalent arrays.

Experimental observations are compared to theoretical predictions based on kinetic Monte Carlo simulations [26], using the point-dipole Hamiltonian of Eq. (1) and the model of thermally assisted moment reorientation described by Eq. (2).

For the simulations, a lattice parameter of $a=600$ nm is used (Fig. 1), the volume magnetization is set to $M_S = 350 \times 10^3 \text{ A m}^{-1}$ (corresponding to approximately $9 \times 10^6 \mu_B$ per nanomagnet moment), the attempt frequency to $\nu_0 = 10^9 \text{ s}^{-1}$, and the single-nanomagnet switching barrier to $E_b = 0.626 \text{ eV}$ [23,26]. The temperature for kinetic Monte Carlo simulations is set to 460 K. For the visualization of state network diagrams, the same values of a , M_S , ν_0 , and E_b are used with transition rates calculated for $T=400$ K.

For the kinetic Monte Carlo simulations, we include a small effective bias magnetic field (\mathbf{H}_{bias}) of approximately $50 \mu\text{T}$ along the direction shown in Fig. 2. This small bias field influences the relaxation rates to a specific low-energy state and is critical to obtain simulated transition probabilities that agree with the experimental observations. The presence of such a field in the XPEEM chamber was also observed in other experiments [27].

IV. RESULTS AND DISCUSSION

A. Probabilistic operations

We begin by presenting the relaxation dynamics of the design shown in Fig. 2(a), which we refer to as a probabilistic logic gate or P gate. Starting from a field-set state S_0 [Fig. 2(b)] and following thermal relaxation at approximately 290°C for 2 h for a gate with approximately 5-nm-thick nanomagnets, we find that, of the 390 P gates tested, 24.6% of the gates reached the ground state G1 [Fig. 2(c)] and 48.5% of the gates ended up in the degenerate ground state G2 [Fig. 2(d)]. In addition, several other states are observed after relaxation, most notably the metastable state M in Fig. 2(e), which accounts for 16% of the final configurations.

The lower probability of reaching G1 as compared to G2 indicates that the transition barriers toward G1 must be higher than those that occur on the path toward G2. This

result is illustrated in the state network diagram in Fig. 2(f). Here, the fastest paths from S_0 toward G1 and G2, represented by the larger black points, are highlighted in blue and red, respectively. Both paths include three moment reversals and are of the intermittent type. The first transition on the path toward G1 (in blue) requires a higher thermal activation energy than the one toward G2 (in red), thus biasing the system toward G2.

The relaxation dynamics characterizing the exploration of competing relaxation paths by the P gate is experimentally shown in the image sequence in Fig. 2(g), where individual moment reorientations during relaxation are imaged, and is indicated by the path highlighted in green in Fig. 2(f). Here, the P gate is field-set [Image 1 in Fig. 2(g)] with a magnetic field applied in the opposite direction (180°) to the field applied in Fig. 2(b). During the course of relaxation, the P gate encounters a metastable state corresponding to the second image in Fig. 2(g). Its course is then reversed by traveling back to the initial state and, finally, it traverses the path to G2.

In summary, intermittent paths in the state network diagram result in probabilistic relaxation. The direction of the applied field is also important since this defines the initial state and thus the subsequent energy landscape. Finally, it should be pointed out that the intermittent relaxation path for the P gate is a result of the incorporation of the four-vertex structure shown in Fig. 1(e) into the gate design, which leads to the creation of a charge at the vertex as the gate transitions from an initial field-set state to the final low-energy state during the course of thermal relaxation.

B. Deterministic operations

Deterministic relaxation toward a specific ground state can be realized by introducing the four-loop structure shown in Fig. 1(a) into the design to give a monotonic relaxation path. To demonstrate this idea, we use the structure shown in Fig. 3(a), which we refer to as a deterministic logic gate or D gate. With the D gate, we previously demonstrated Boolean operations, with more than 90% of D gates experimentally observed to relax to the G1 state shown in Fig. 3(b) [17]. The high operational reliability of the D gate results from that fact that the first relaxation step from the initial field-set state S_0 [Fig. 3(a)] toward the low-energy state G1 [Fig. 3(b)] has a lower energy barrier than the first transition on the relaxation path toward the low-energy state G2 [Fig. 3(c)]. Therefore, although the path toward G1 requires six moment reversals, compared with the five reversals required to reach G2, the system is kinetically biased to relax toward G1 (see the supplementary data in Ref. [17]).

In summary, structures with monotonic paths in the state network diagram result in deterministic relaxation. Even though the D gate has two vertex structures, not all vertex charge creation leads to an increase in energy of the D gate,

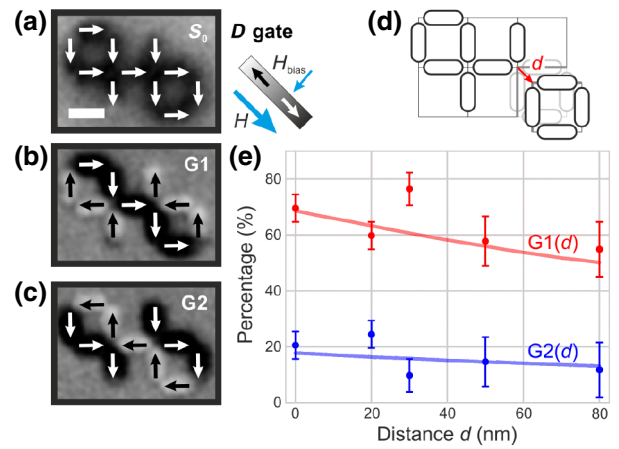


FIG. 3. Tuning of ground-state occupation with modification of the nanomagnetic design. XPEEM images of (a) the field-set initial state S_0 of the original D -gate design and the ground states (b) G1 and (c) G2. The scale bar in (a) measures 500 nm and moment orientations are indicated with black and white arrows. (d) Schematic drawing of the D gate. In order to tune the probability of structures reaching the ground state G1, the lower right four-loop structure is moved by the distance d . (e) The percentage of gates ending up in the two ground states G1 and G2 for a four-loop structure offset by a distance d . The final percentages of low-energy states in 51 gates for different distances (points) are compared with the kinetic Monte Carlo simulations (solid lines).

as the change in energy during charge creation is counterbalanced by the lowering of the dipolar energy in the two four-loop structures.

C. Continuous modulation of output

The relaxation outcome of the D gate can be modified by physically altering its design. This modification can be achieved by changing the position of one of the two four-loop structures so that it is at different distances d away from the vertex point [see Fig. 3(d)]. Increasing d results in a weakening of the dipolar coupling between one of the four-loop structures and rest of the gate, leading to a higher probability of accessing non-ground-state low-energy states along the path toward G1 and thereby reducing the final percentages of low-energy states, p_{G1} .

We tested the thermal relaxation behavior for different distances d between 0 and 80 nm for 51 modified D gates for each d . It should be noted that the thermal protocol was different than that used in our earlier experiments [17]. Because of experimental constraints, a maximum temperature of $T \sim 190^\circ\text{C}$ was used along with a thickness of approximately 3 nm for the nanomagnets and only a relaxation time of 1 h, as opposed to $T \sim 290^\circ\text{C}$, nanomagnet thickness of approximately 5 nm, and a relaxation time of 2 h. Because of the limited time, it should be noted that the D gates with $d=0$ nm did not reach G1 with 100% success. The percentages p_{G1} and p_{G2} of ground states

G1 and G2, as a function of separation d , are plotted as points in Fig. 3(e). We observe a decrease of $p_{G1}(d)$ with increasing d from approximately 70% at 0 nm to approximately 55% at 80 nm and less variation with d for $p_{G2}(d)$. These percentages for the modified D gates are compared with kinetic Monte Carlo simulations [solid lines in Fig. 3(e)], which reproduce the experimental results well with the available statistics using the parameters given in the methods section. This result demonstrates that the target probabilities can be controlled by physically modifying the gate design.

D. Extended circuits

So far, we have discussed the relaxation behavior of individual computational building blocks containing a few nanomagnets each. To create extended circuits capable of advanced calculations, such as adders or artificial neural networks, the individual gates need to be combined into larger structures.

In order to integrate more than one gate into a larger circuit, several conditions need to be met. First, each individual logic gate requires two or more input magnets and an output magnet. Second, the input and output magnets of different gates need to be at a location that allows them to be linked to neighboring gates. Third, there needs to be a strong coupling between the output magnet of one gate and the input magnet of the next gate. Finally, their respective

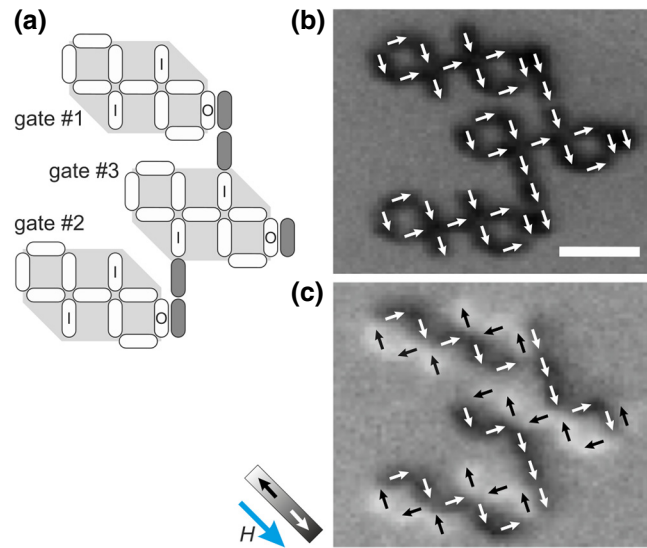


FIG. 4. Connecting several D gates. (a) Three equivalent D gates (highlighted in light gray) are coupled by strongly interacting parallel nanomagnets (in dark gray). These nanomagnets link the output magnets (O) of the outer two gates 1 and 2 to the input magnets (I) of the middle gate 3. (b) Initial field-set state and (c) final state imaged with XPEEM. After thermal relaxation, the outer gates 1 and 2 relax to the ground state G1, and the central gate 3 relaxes to G2. The scale bar in (b) measures $1 \mu\text{m}$. Moment orientations are indicated with black and white arrows.

relaxation kinetics, which govern their operational reliability, should remain largely unaffected when the gates are linked together.

An experimental realization of three D gates connected by linear chains of strongly coupled nanomagnets is shown in Fig. 4. Starting from the field-set state in Fig. 4(b) and after implementing the same thermal protocol as that used for the gates discussed in Sec. IV C, the extended circuit relaxes into one of its degenerate ground states, as shown in Fig. 4(c). Here, the top and bottom D gates, 1 and 2, relax into the ground state G1, whereas the middle, constrained D gate, 3, relaxes into G2. The stability of the individual D gates and the effect of constrained input moments on the relaxation behavior of a D gate have been discussed in Ref. [17]. The result shown in Fig. 4 for three connected D gates thus provides a first proof of concept for integrating logic gates into extended arrays for use in large circuits.

V. CONCLUSIONS

In this work, we show how different relaxation pathways can be engineered in artificial spin ice structures comprising arrays of dipolar-coupled nanomagnets for deterministic and probabilistic computation. We identify two distinct categories of relaxation pathways, which can be (1) monotonic and (2) intermittent, and are visualized using a nanomagnetic state network diagram.

The implementation of loop-based designs in the D gates, which favors monotonic relaxation pathways, greatly improves the reliability of Boolean logic gates as demonstrated previously [17]. In contrast, intermittent relaxation pathways such as those of P gates and often associated with the creation of energetically unfavorable vertex charges, lead to different probabilities of low-energy states, as the system can explore competing relaxation pathways. The different probabilities to reach particular low-energy states could be exploited in weighted computational schemes such as artificial neural networks.

We also demonstrate that the probability of low-energy states can be tuned by changing the logic gate design. This design also depends on, for example, the direction of the applied magnetic field used to set the initial state of different gates. This control could also be achieved *in situ*, for example, with Oersted fields in a current-carrying nanowire [28] or by exploiting strain-mediated effects [9]. Such schemes would even provide a means to vary the transition barriers between or even during computational (i.e., relaxation) cycles.

Finally, the integration of individual logic gates into extended circuits opens the possibility for implementation in both conventional computation [4] and in novel computational schemes such as those involving mapping a problem to a magnetic Hamiltonian [13,29]. The raw data that support this study is available via the Zenodo repository [30].

ACKNOWLEDGMENTS

This work is supported by the Swiss National Science Foundation (SNSF). The XPEEM experiments are performed at the Surface/Interface: Microscopy (SIM) beamline of the Swiss Light Source, Paul Scherrer Institute, Villigen, Switzerland. H.A. and N.L. are supported by SNSF Grants No. 200021_155917 and No. 200020_172774. D.S. receives partial funding via a PSICROSS proposal (Grant No. 03.15). J.V. is supported by SNSF Grant No. 200021_153540. J.C. receives funding from the European Union's Horizon 2020 research and innovation program under the Marie Skłodowska-Curie Grant No. 701647.

-
- [1] A. Imre, G. Csaba, L. Ji, A. Orlov, G. H. Bernstein, and W. Porod, Majority logic gate for magnetic quantum-dot cellular automata, *Science* **311**, 205 (2006).
- [2] R. P. Cowburn and M. E. Welland, Room temperature magnetic quantum cellular automata, *Science* **287**, 1466 (2000).
- [3] B. Lambson, D. Carlton, and J. Bokor, Exploring the Thermodynamic Limits of Computation in Integrated Systems: Magnetic Memory, Nanomagnetic Logic, and the Landauer Limit, *Phys. Rev. Lett.* **107**, 010604 (2011).
- [4] M. T. Niemier, G. H. Bernstein, G. Csaba, A. Dingler, X. S. Hu, S. Kurtz, S. Liu, J. Nahas, W. Porod, M. Siddiq, and E. Varga, Nanomagnet logic: progress toward system-level integration, *J. Phys. Condens. Matter* **23**, 493202 (2011).
- [5] R. L. Stamps, S. Breitkreutz, J. Akerman, A. V. Chumak, Y. Otani, G. E. W. Bauer, J. Thiele, M. Bowen, S. A. Majetich, M. Klaui, I. L. Prejbeanu, B. Dieny, N. M. Dempsey, and B. Hillebrands, The 2014 magnetism roadmap, *J. Phys. D* **47**, 333001 (2014).
- [6] J. Hong, B. Lambson, S. Dhuey, and J. Bokor, Experimental test of Landauer's principle in single-bit operations on nanomagnetic memory bits, *Sci. Adv.* **2**, e1501492 (2016).
- [7] L. Gross, R. R. Schlittler, G. Meyer, and R. Allenspach, Magnetologic devices fabricated by nanostencil lithography, *Nanotechnology* **21**, 325301 (2010).
- [8] S. Breitkreutz, J. Kiermaier, I. Eichwald, X. Ju, G. Csaba, D. Schmitt-Landsiedel, and M. Becherer, Majority gate for nanomagnetic logic with perpendicular magnetic anisotropy, *IEEE Trans. Magn.* **48**, 4336 (2012).
- [9] N. D'Souza, M. Salehi Fashami, S. Bandyopadhyay, and J. Atulasimha, Experimental clocking of nanomagnets with strain for ultralow power boolean logic, *Nano Lett.* **16**, 1069 (2016).
- [10] D. Bhowmik, L. You, and S. Salahuddin, Spin Hall effect clocking of nanomagnetic logic without a magnetic field, *Nat. Nanotechnol.* **9**, 59 (2013).
- [11] E. Irina, B. Stephan, Z. Grazvydas, C. György, P. Wolfgang, and B. Markus, Majority logic gate for 3D magnetic computing, *Nanotechnology* **25**, 335202 (2014).
- [12] Z. Gu, M. E. Nowakowski, D. B. Carlton, R. Storz, M.-Y. Im, J. Hong, W. Chao, B. Lambson, P. Bennet, M. T. Alam, M. A. Marcus, A. Doran, A. Young, A. Scholl, P. Fischer, and J. Bokor, Sub-nanosecond signal propagation in anisotropy-engineered nanomagnetic logic chains, *Nat. Commun.* **6**, 6466 (2015).
- [13] S. Bhanja, D. K. Karunaratne, R. Panchumarthy, S. Rajaram, and S. Sarkar, Non-Boolean computing with nanomagnets for computer vision applications, *Nat. Nanotechnol.* **11**, 177 (2015).
- [14] B. Sutton, K. Y. Camsari, B. Behin-Aein, and S. Datta, Intrinsic optimization using stochastic nanomagnets, *Sci. Rep.* **7**, 44370 (2017).
- [15] R. F. Wang, C. Nisoli, R. S. Freitas, J. Li, W. McConville, B. J. Cooley, M. S. Lund, N. Samarth, C. Leighton, V. H. Crespi, and P. Schiffer, Artificial 'spin ice' in a geometrically frustrated lattice of nanoscale ferromagnetic islands, *Nature* **439**, 303 (2006).
- [16] E. Mengotti, L. J. Heyderman, A. Fraile Rodríguez, A. Bisig, L. Le Guyader, F. Nolting, and H. B. Braun, Building blocks of an artificial kagome spin ice: Photoemission electron microscopy of arrays of ferromagnetic islands, *Phys. Rev. B* **78**, 144402 (2008).
- [17] H. Arava, P. M. Derlet, J. Vijayakumar, J. Cui, N. S. Bingham, A. Kleibert, and L. J. Heyderman, Computational logic with square rings of nanomagnets, *Nanotechnology* **29**, 265205 (2018).
- [18] R. V. Chopdekar, G. Duff, R. V. Hügli, E. Mengotti, D. A. Zanin, L. J. Heyderman, and H. B. Braun, Controlling vortex chirality in hexagonal building blocks of artificial spin ice, *New J. Phys.* **15**, 125033 (2013).
- [19] Y.-L. Wang, Z.-L. Xiao, A. Snezhko, J. Xu, L. E. Ocola, R. Divan, J. E. Pearson, G. W. Crabtree, and W.-K. Kwok, Rewritable artificial magnetic charge ice, *Science* **352**, 962 (2016).
- [20] J. C. Gartside, D. M. Arroo, D. M. Burn, V. L. Bemmer, A. Moskalenko, L. F. Cohen, and W. R. Branford, Realization of ground state in artificial kagome spin ice via topological defect-driven magnetic writing, *Nat. Nanotechnol.* **13**, 53 (2018).
- [21] P. Gypens, J. Leliaert, and B. Van Waeyenberge, Balanced Magnetic Logic Gates in a Kagome Spin Ice, *Phys. Rev. Appl.* **9**, 034004 (2018).
- [22] F. Caravelli and C. Nisoli, *Computation via Interacting Magnetic Memory Bites: Integration of Boolean Gates* (2018), arXiv:1810.09190v2.
- [23] S. Liashko, H. Jónsson, and V. Uzdin, The effect of temperature and external field on transitions in elements of kagome spin ice, *New J. Phys.* **19**, 113008 (2017).
- [24] A. Farhan, A. Kleibert, P. M. Derlet, L. Anghinolfi, A. Balan, R. V. Chopdekar, M. Wyss, S. Gliga, F. Nolting, and L. J. Heyderman, Thermally induced magnetic relaxation in building blocks of artificial kagome spin ice, *Phys. Rev. B* **89**, 214405 (2014).
- [25] L. Le Guyader, A. Kleibert, A. Fraile Rodríguez, S. El Moussaoui, A. Balan, M. Buzzi, J. Raabe, and F. Nolting, Studying nanomagnets and magnetic heterostructures with X-ray PEEM at the Swiss Light Source, *J. Electron. Spectrosc.* **185**, 371 (2012).
- [26] A. Farhan, P. M. Derlet, A. Kleibert, A. Balan, R. V. Chopdekar, M. Wyss, J. Perron, A. Scholl, F. Nolting, and L. J. Heyderman, Direct Observation of Thermal

- Relaxation in Artificial Spin Ice, *Phys. Rev. Lett.* **111**, 057204 (2013).
- [27] S. Gliga, G. Hrkac, C. Donnelly, J. Buchi, A. Kleibert, J. Cui, A. Farhan, E. Kirk, R. V. Chopdekar, Y. Masaki, N. S. Bingham, A. Scholl, R. L. Stamps, and L. J. Heyderman, Emergent dynamic chirality in a thermally driven artificial spin ratchet, *Nat. Mater* **16**, 1106.
- [28] J. Kiermaier, S. Breitzkreutz, G. Csaba, D. Schmitt-Landsiedel, and M. Becherer, Electrical input structures for nanomagnetic logic devices, *J. Appl. Phys.* **111**, 07E341 (2012).
- [29] A. Lucas, Ising formulations of many NP problems, *Front. Phys.* **2**, 5 (2014).
- [30] H. Arava, N. Leo, D. Schildknecht, J. Cui, J. Vijayakumar, P. M. Derlet, A. Kleibert, and L. J. Heyderman, Data for: “Engineering relaxation pathways in building blocks of artificial spin ice for computation,” <https://doi.org/10.5281/zenodo.2649141> (2019).